The influence of vegetation water dynamics on the ASCAT backscatter-incidence angle relationship in the Amazon

Ashwini Petchiappan[1], Susan C. Steele-Dunne[2], Mariette Vreugdenhil[3], Sebastian Hahn[3], Wolfgang Wagner[3], and Rafael Oliveira[4]

[1]Department of Water Management, Delft University of Technology, Stevinweg 1, Delft 2600 GA, The Netherlands
[2]Department of Geoscience and Remote Sensing, Delft University of Technology, Stevinweg 1, Delft 2600 GA, The Netherlands
[3]Department of Geodesy and Geo-Information, TU Wien, Vienna 1040, Austria
[4]Department of Plant Biology, Institute of Biology P.O.Box: 6109, University of Campinas – UNICAMP 13083-970, Campinas, SP, Brazil

Correspondence: Susan Steele-Dunne (s.c.steele-dunne@tudelft.nl)

1   **Abstract.** Microwave observations are sensitive to plant water content and could therefore provide essential information on
2   biomass and plant water status in ecological and agricultural applications. The combined data record of the C-band scatterom-
3   eters on ERS 1/2, the Metop series and the planned Metop Second Generation satellites will span over 40 years, which would
4   provide a long-term perspective on the role of vegetation in the climate system. Recent research has indicated that the unique
5   viewing geometry of ASCAT could be exploited to observe vegetation water dynamics. The incidence angle dependence of
6   backscatter can be described with a second order polynomial, the slope and curvature of which are related to vegetation. In a
7   study limited to grasslands, seasonal cycles, spatial patterns and interannual variability in the slope and curvature were found
8   to vary among grassland types and were attributed to differences in moisture availability, growing season length and pheno-
9   logical changes. To exploit ASCAT slope and curvature for global vegetation monitoring, their dynamics over a wider range
10   of vegetation types needs to be quantified and explained in terms of vegetation water dynamics. Here, we compare ASCAT
11   data with meteorological data and GRACE Equivalent Water Thickness (EWT) to explain the dynamics of ASCAT backscat-
12   ter, slope and curvature in terms of moisture availability and demand. We consider differences in the seasonal cycle, diurnal
13   differences, and the response to the 2010 and 2015 droughts across ecoregions in the Amazon basin and surroundings. Results
14   show that spatial and temporal patterns in backscatter reflect moisture availability indicated by GRACE EWT. Slope and cur-
15   vature dynamics vary considerably among the ecoregions. The evergreen forests, often used as a calibration target, exhibit very
16   stable behaviour even under drought conditions. The limited seasonal variation follows changes in the radiation cycle, and may
17   indicate phenological changes such as litterfall. In contrast, the diversity of land cover types within the Cerrado region results
18   in considerable heterogeneity in terms of the seasonal cycle and the influence of drought on both slope and curvature. Seasonal
19   flooding in forest and savanna areas also produced a distinctive signature in terms of the backscatter as a function of incidence
20   angle. This improved understanding of the incidence angle behaviour of backscatter increases our ability to interpret and make
21   optimal use of the ASCAT data record and VOD products for vegetation monitoring.

1 Introduction

23 Microwave remote sensing observations are sensitive to plant water content, which depends on above ground biomass and

24 plant water status (Konings et al., 2019). Data from active and passive microwave sensors can provide valuable information

25 about vegetation in a range of applications in ecological and agricultural monitoring (Konings et al., 2019; Steele-Dunne et al.,

26 2017). In particular, Vegetation Optical Depth (VOD) products derived from various passive and active microwave sensors are

27 increasingly used for biomass monitoring (Liu et al., 2015), drought monitoring (Liu et al., 2018), wildfire risk assessment

28 (Forkel et al., 2019) and have been related to Gross Primary Production (Teubner et al., 2018, 2019), carbon stocks (Chaparro

29 et al., 2019) and drought-driven tree mortality (Rao et al., 2019). Currently VOD datasets are available from single sensor

30 passive microwave observations, such as SMAP (Konings et al., 2016), SMOS (Fernandez-Moran et al., 2017) and AMSR2

31 (Owe et al., 2001; De Jeu, 2003). Furthermore, long-term data records are available that combine VOD from different sensors

32 (Moesinger et al., 2020; Liu et al., 2011).

33 The current study is motivated by the availability of consistent C-band data from 1991 to at least 2030, and its potential

34 value as a long-term data record for vegetation monitoring. The Advanced Scatterometer (ASCAT) is a real aperture radar

35 operating at 5.255 GHz with VV polarization. There are currently three ASCAT instruments in orbit on Metop-A, Metop-B

36 and Metop-C, launched in October 2006, September 2012 and November 2018 respectively. ASCAT builds on the success

37 of the European Scatterometer (ESCAT) which flew on the ERS-1/2 satellites from 1991-2011 (Attema, 1991; Figa-Saldaña

38 et al., 2002; Wagner et al., 2013)). Continuation of the ESCAT/ASCAT record is ensured by the plans to launch SCA on

39 Metop-SG in 2024 (Stoffelen et al., 2017). Using data from a single series of satellites with identical and inter-calibrated

40 instruments circumvents many of the challenges of reconciling data using different frequencies, viewing geometries and orbit

41 characteristics. The continuity from ERS to Metop and Metop-SG ensures an internally consistent data product for at least 40

42 years, rendering it ideal to study the role of vegetation in the climate system.

43 Many early studies demonstrated the sensitivity of ESCAT and ASCAT backscatter to vegetation, and explored the potential

44 value of these data for vegetation monitoring (Wismann et al., 1995; Frison et al., 1998; Woodhouse et al., 1999; Jarlan et al.,

45 2002; Steele-Dunne et al., 2012; Schroeder et al., 2016). These studies focused on spatial and temporal variations in backscatter

46 normalized to some reference angle. Here, the focus is on the potential information content of the incidence angle behaviour

47 of backscatter, and particularly the so-called "Dynamic Vegetation Parameters" describing the incidence angle behaviour of

48 backscatter as calculated in the TU Wien Soil Moisture Retrieval (TUW SMR) algorithm (Hahn et al., 2017).

49 The ASCAT Dynamic Vegetation Parameters refer to the parameters of the second order Taylor polynomial used to describe

50 the incidence angle (θ) dependence of backscatter σ°. This is described as follows:

51
$$\sigma^\circ(\theta) = \sigma^\circ(\theta_r) + \sigma'(\theta_r) \cdot (\theta - \theta_r) + \frac{1}{2} \cdot \sigma''(\theta r) \cdot (\theta - \theta_r)^2 \qquad [dB] \qquad (1)$$

52 where $\sigma^\circ(\theta_r)$, $\sigma'(\theta_r)$ and $\sigma''(\theta_r)$ are the normalized backscatter, slope and curvature at some reference angle θ_r. In the

53 TUW SMR, this expression is used to normalize backscatter values from different incidence angles to a reference angle θ_r. It is

54 also used to account for the influence of vegetation on backscatter as the incidence angle behaviour of σ° depends on whether

55 total backscatter is dominated by surface scattering from the soil, volume scattering from the vegetation, or multiple scattering
56 (Wagner et al., 1999; Naeimi et al., 2009; Hahn et al., 2017).

57   Results from Steele-Dunne et al. (2019) suggest that considering the slope ($\sigma'(\theta)$) and curvature ($\sigma''(\theta)$) dynamics in combi-
58 nation with the backscatter could yield valuable insights into vegetation water dynamics. Seasonal cycles, spatial patterns and
59 interannual variability in the slope varied between grassland cover type reflecting variations in soil moisture availability and
60 growing season length. Results also suggested that curvature variations were influenced by the total water content, but also its
61 vertical distribution within the vegetation and the geometry of constituents. Contiguous anomalies were observed in both slope
62 and curvature during drought periods, suggesting that the slope and curvature provide insight into when the severity of a soil
63 moisture anomaly is enough to impact vegetation. Diurnal variations were also observed and attributed to sub-daily variations
64 in the dominant scattering mechanism due to changes in the vertical moisture distribution of the grasses. More recently, Pfeil
65 et al. (2020) observed a "spring peak" in slope values around April in broadleaf deciduous forest in Europe. Using LAI and
66 data from the Pan European Phenological database (PEP725) (Templ et al., 2018) they argued that this spring peak in ASCAT
67 slope coincides with spring activation, particularly the increase in water content of bare twigs and branches prior to leaf out in
68 broadleaf deciduous forests. ASCAT slope and curvature therefore seem to be sensitive to changes in vegetation water content
69 and structure of vegetation.

70   The goal of this study is to improve our understanding of the ASCAT backscatter-incidence angle relationship and how
71 they might be used to monitor vegetation water dynamics. The Amazon basin and its surroundings has been chosen as a study
72 area as it provides a wide range in terms of expected variability in ASCAT backscatter, slope and curvature. Backscatter in
73 the evergreen forest was considered so stable that this region has been used for satellite radar calibration (Birrer et al., 1982).
74 In contrast, seasonal changes in the Cerrado are expected to yield strong annual cycles in backscatter, slope and curvature.
75 Seasonal cycles and diurnal differences in ASCAT backscatter, slope and curvature will be determined for several ecoregions
76 of interest. These will be compared to meteorological data and GRACE terrestrial water storage variations to relate the ASCAT
77 backscatter, slope and curvature to moisture availability and demand. Finally, we will investigate whether there are anomalies
78 in the ASCAT backscatter, slope and curvature as a result of the 2010 and 2015 droughts.

2 Data and Methods

2.1 Study Area

81 Figure 1 shows the extent of the study domain, highlights the biomes (by color) and outlines the ecoregions of interest identified
82 in the WWF Terrestrial Ecoregions dataset (WWF, 2019) and described by Olson et al. (2001). The study domain extends from
83 9°N to 19°S, and 44°W to 80°W. Most of the study region is covered by the Amazon rain forest, which extends over 5.3
84 million km^2 (Soares et al., 2006). Six forest ecoregions are investigated here:
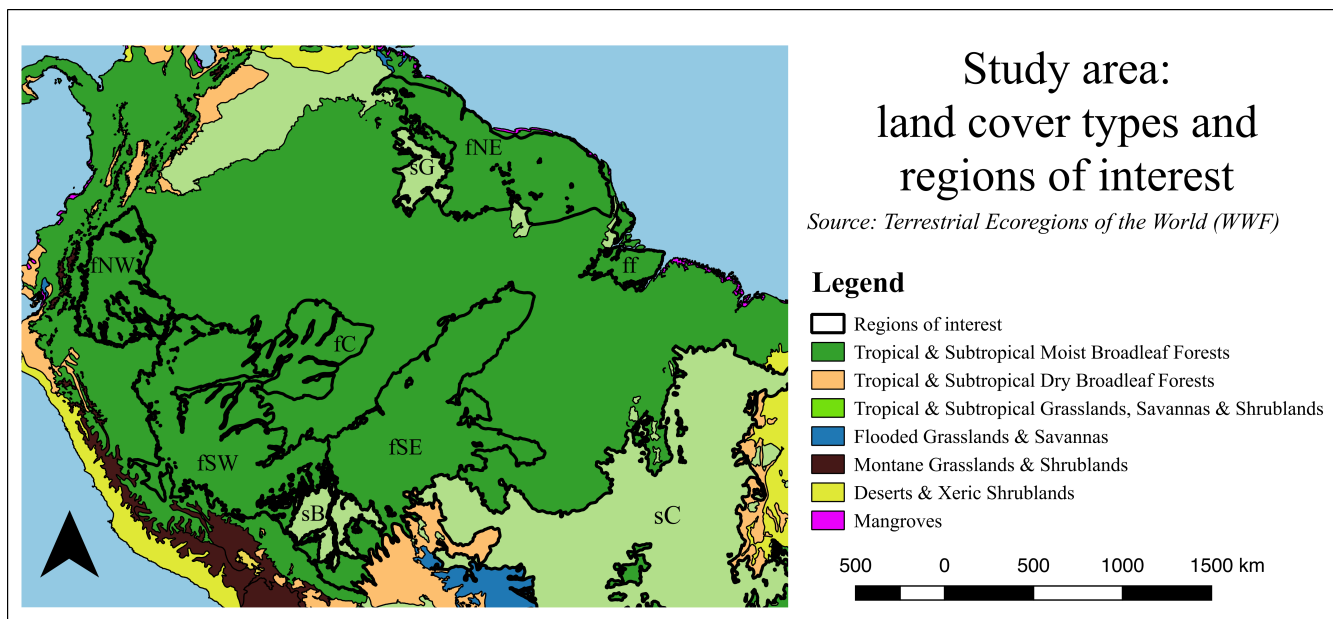
Figure 1. Study Area. The map is colored by biome, and nine ecoregions of interest are highlighted based on the dataset of Olson et al. (2001). The six forest ecoregions of interest are Napo moist forest (fNW), Guianan moist forests (fNE), Southwest Amazon moist forests (fSW), Madeira-Tapajos moist forest (fSE), Jurua-Perez moist forests (fC) and the Marajo Varzea flooded forests (ff). The three savanna ecoregions of interest are the Cerrado (sC), Guianan Savanna (sG) and Beni Savanna (sB).

1. The Napo moist forests (fNW), located in northwest Amazonia, receive some of the highest amounts of annual precipitation in the biome, reaching up to 4000 mm in some parts. This highly biodiverse region has canopies reaching 40 m.

2. The Guianan moist forests (fNE) are one of the largest continuous stretches of relatively pristine lowland tropical rainforest in the world. There are two distinct wet seasons: from December to January and from May to August. The floral diversity is rich, with multi-tiered vegetation of 40 m tall trees with herbaceous plants below. The dry season (September-November) can see a substantial reduction in leaves, although the forest is evergreen.

3. The Southwest Amazon moist forests (fSW) have significant variations in topography and soil characteristics, leading to extremely high biodiversity. The size and orientation of the ecoregion means that climatic conditions vary markedly – the north being wetter and having less seasonal variability compared to the south. The inaccessibility of the region has aided in its conservation.

4. The Madeira-Tapajós moist forests (fSE) are transected by the Transamazon Highway, and have high levels of urbanization and deforestation. There are characteristic liana (woody vine) forests with a lower (< 25 m) and more open canopy than the typical humid terra firme forests.

5. The Juruá-Perez moist forests (fC) are largely intact forests in the low Amazon Basin. The canopy can reach up to 30 m, with some patches of open canopy.

6. The seasonally flooded forest, Marajó várzea (ff), is located at the mouth of the Amazon River. The vegetation is dominated by palms, and shorter than surrounding forests. It has areas with tidal flows from the Atlantic Ocean, as well as seasonally and permanently inundated forests. The annual seasonal flooding occurs during the peak precipitation period between January-May (Camarão et al., 2002).

Three savanna ecoregions are also considered in this study:

1. The Cerrado (sC) borders the Amazon biome to the southeast. It occupies an area of 2 million km^2 in the Brazilian Central Plateau and is the second most extensive biome in South America (Oliveira et al., 2005). The vegetation cover varies from closed tree canopy to grasslands with low shrubs only (Eiten, 1972).

2. The Guianan savanna (sG) consists of forest patches encircled by extensive grasslands and shrub formations. The area is more susceptible to vegetation fires than typical humid moist forest environments and the dry season lasts from December-March.

3. The Beni savanna (sB) is a wetland region with riverine gallery forests and small forest islands. The landscape is dominated by the palm species Attalea princeps (Hordijk et al., 2019). Seasonal flooding occurs in up to half the region for 4 to 9 months, peaking in March-April (Hamilton et al., 2004).

Three Köppen-Geiger Climate Classes (KGCC) cover most of the study region (Fig. 2). The evergreen forest regions are classified as Af (tropical fully humid) or Am (tropical monsoonal), and the savanna regions have Aw (tropical winter dry) climate (Bradley et al., 2011). The annual precipitation in the forests can exceed 2000-3000 mm, with less than 100 mm rainfall for up to three months in the year. The savannas have a wet season extending for 5-8 months, with an annual total of 1000-2000 mm (Bradley et al., 2011). Net radiation peaks in the winter months, due to the absence of cloud cover in the dry season (Liu et al., 2018). Two major droughts occurred in the region during the study period, in 2010 and 2015 (Jiménez-Muñoz et al., 2016; Marengo et al., 2011) and are of particular interest in this study.

2.2 ASCAT data

The Advanced Scatterometer (ASCAT) data were processed using the same procedure as Steele-Dunne et al. (2019). Metop-A ASCAT SZR Level 1b Fundamental Climate Data Record, resampled at a 12.5 km swath grid, were obtained from the EUMETSAT Data Centre for the period 2007 to 2016. Following the procedure described by Naeimi et al. (2009), the backscatter observations were resampled to a fixed Earth grid using a Hamming window function. The slope and curvature were calculated from the ASCAT backscatter observations using the method introduced by Metzler (2013) and described by Hahn et al. (2017). The ASCAT instrument on-board the Metop satellites has three antennas on either side, oriented at 45° (fore), 90° (mid) and 135° (aft) to the satellite track. As a result, three independent measurements of each location on the surface are obtained almost
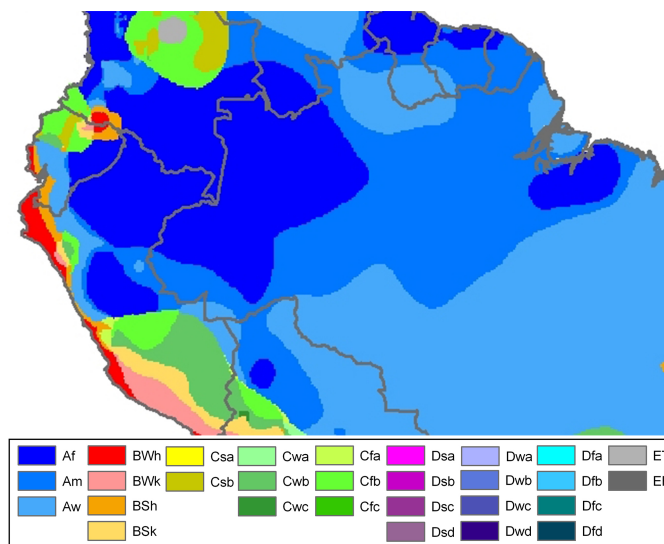
Figure 2. Köppen-Geiger climate zones in the study area (Source: (Peel et al., 2007)).

130 instantaneously. These so-called "backscatter triplets" (Hahn et al., 2017) are used to calculate an instantaneous backscatter

131 slope, also known as the "local slope":

$$\sigma'\left(\frac{\theta_{mid} - \theta_{a/f}}{2}\right) = \frac{\sigma^{\circ}_{mid}(\theta_{mid}) - \sigma^{\circ}_{a/f}(\theta_{a/f})}{\theta_{mid} - (\theta_{a/f})} \qquad [dB/deg] \tag{2}$$

133 where *mid*, *a* and *f* indicate the backcatter measurements from the mid-, aft- and fore-beams respectively. Following the

134 approach of Metzler (2013), an Epanechnikov kernel (with width λ=21) is used to weight the local slope values by their

135 temporal distance from a given day of interest. This yields an estimate of slope and curvature for a given day, based on all local

136 slope values within a 42-day window. For a more detailed description of their derivation, the reader is referred to Steele-Dunne

137 et al. (2019).

138 Observations from the descending and ascending overpasses are unlikely to occur on the same day. Hence, the σ°_{40} data were

139 aggregated into 10-day intervals (dekads). Unless otherwise indicated, the analysis uses data from the descending pass only ($\sim$

140 10 am). Diurnal differences refers to the values from the descending overpass ($\sim$ 10 am) minus the values from the ascending

141 overpass ($\sim$ 10 pm).

142 2.3 Water Dynamics data

143 Downwelling shortwave radiation at the surface and specific humidity were obtained from the Princeton meteorological dataset

144 (Sheffield et al., 2006). These data have a $0.5° \times 0.5°$ daily resolution. Precipitation data were obtained from the Global

145 Precipitation Climatology Product (GPCP) Precipitation Level 3 Monthly 0.5-Degree V3.0 beta dataset (Huffman et al., 2009).

146 Data from the Gravity Recovery and Climate Experiment (GRACE) mission were used to provide insight into terrestrial water

147 storage variations (Landerer and Swenson, 2012; Swenson and Wahr, 2006). Here, we used the equivalent water thickness

148 (EWT) from the GRACE Tellus dataset which is available at $1° \times 1°$, monthly resolution from the NASA JPL Physical

149 Oceanography Distributed Active Archive Center (PO DAAC). These data give the relative change in EWT with respect to a

150 baseline, the method of calculation for which is explained by Wahr et al. (1998). These data provide information on fluctuations

151 in EWT on monthly to inter-annual timescales.

152 Seasonal cycles were determined for precipitation, radiation, humidity, and EWT by averaging data from the entire study

153 duration. Anomalies in precipitation during the drought years were also calculated (as drought year values minus climatology)

154 to provide an indicator of the water stress against which to compare the backscatter, slope and curvature anomalies.

3 Results and Discussion

3.1 Seasonal Climatology

157 Figure 3 shows the mean and range of normalized backscatter (σ_{40}°), slope and curvature for the study period (2007-16). In

158 general, the spatial patterns in the mean and range of all three quantities reflect the spatial patterns in land cover expected

159 from Fig. 1. It is striking that even the influence of the riverine network on the vegetation cover is discernible in the maps,

160 particularly that of the mean backscatter (Fig. 3(a)). Striping effects are visible in several of the maps, particularly that of the

161 range in curvature (Fig. 3(f)). This is due to the backscatter observations at the swath edges being available only at very high

162 or very low incidence angles, which skews the calculation of the slope and curvature. This effect is particularly noticeable in

163 forest regions where the natural dynamic range in both quantities is limited.

164 Mean backscatter is highest, with the least variability, in the evergreen forest regions. Mean backscatter is 2-2.5 dB lower

165 in the savanna areas, but the range is up to 3 dB, compared to just 0.5 to 1 dB in the forest. The stability of the forest is also

166 apparent in the maps of slope and curvature. Though there is some variability among the forest ecoregions, the most striking

167 differences in slope and curvature are between the forest and savanna areas. Limited structural and water content changes in

168 the forest canopy result in a limited range of slope and curvature values in the forest ecoregions. The range of both slope and

169 curvature are highest in the Cerrado areas. One interesting feature is the difference in mean slope between the Guianan savanna

170 (sG) in the north and the Cerrado (sC) region in the south. The Guianan savanna, with sparse vegetation, has low mean slope

171 values. The Cerrado, on the other hand, shows mean values higher than the evergreen forests. This is unexpected since slope

172 is generally considered a measure of "vegetation density", and the evergreen forests are much denser than savannas. This will

173 be discussed in detail in Sect. 3.1.1. Seasonal flooding of the Marajó várzea (the seasonally flooded forest) and Beni savannas

174 ensure that both ecoregions have strong seasonal cycles in all three quantities. These will be discussed separately in Sect. 3.1.2.

175 The mean seasonal cycles in backscatter for the ecoregions of interest are compared in Fig. 4 (a). This highlights the contrast

176 between the very stable evergreen forest regions and the flooded forest and savanna areas. The mean backscatter value is high,

177 with limited seasonal amplitude in the evergreen forest regions. In contrast, backscatter is generally low, but also exhibits

178 strong seasonal variations in the flooded forest and savanna areas. Figures 4 (b-f) show the seasonal variation in backscatter

179 for five ecoregions of interest, against the corresponding climatologies of precipitation and EWT. In all of the ecoregions, the
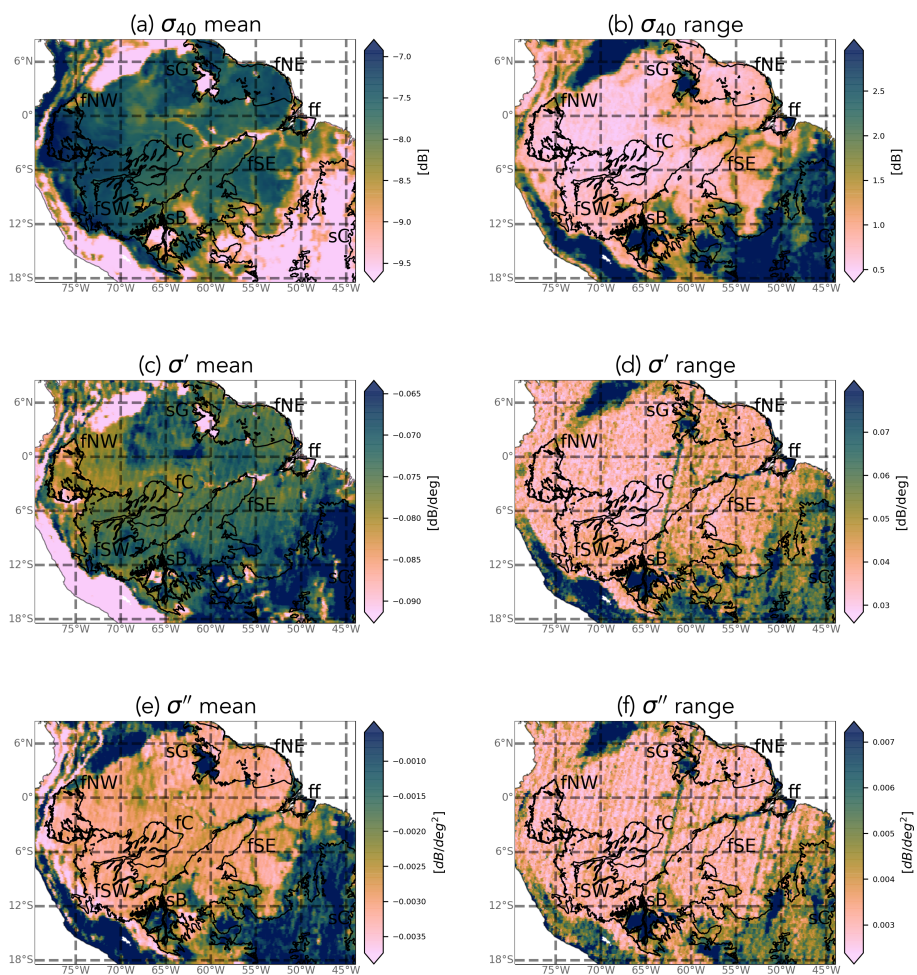
Figure 3. Mean and range of ASCAT normalized backscatter, slope and curvature in the study period (2007-16). Note that there are no data gaps, so white indicates that the quantity has a value equal to or less than the minimum value indicated on the colorbar.
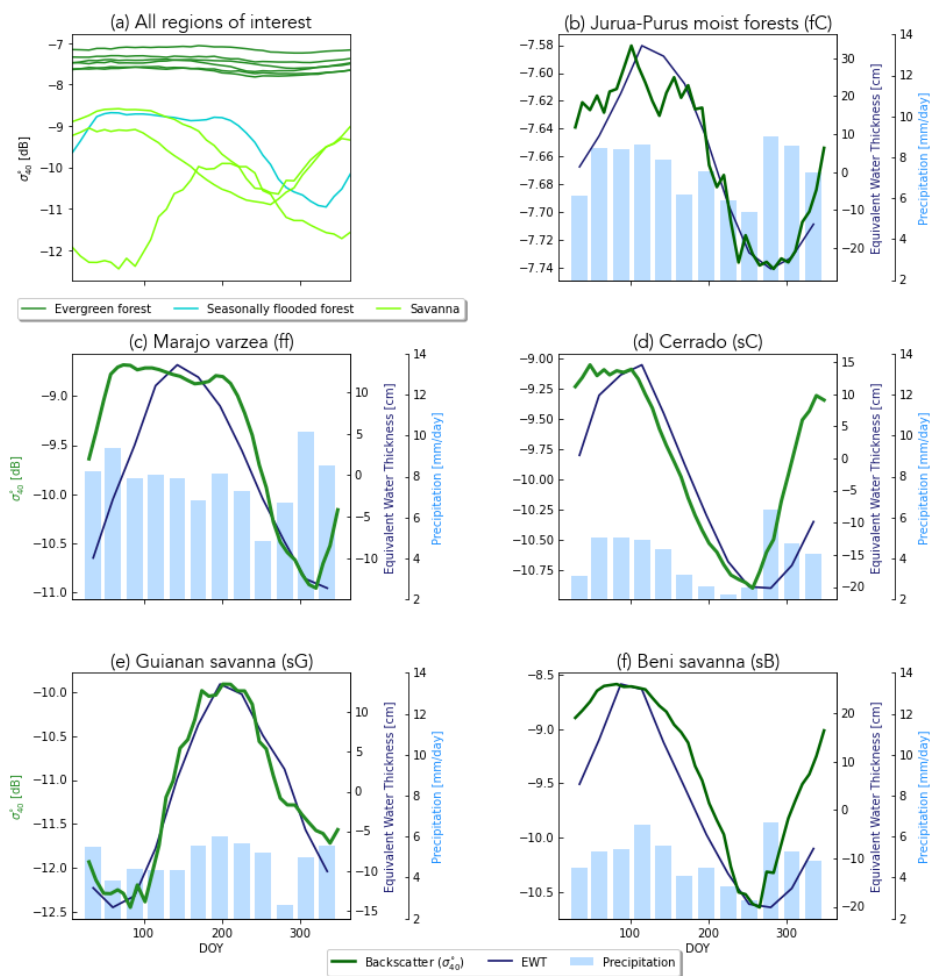
Figure 4. Climatology of backscatter (green line), precipitation (bars), and EWT (blue line) for different cover types.

maximum backscatter occurs during the wet season, and a decrease in backscatter is observed during the dry season, though the amplitude of the variations is obviously much smaller in the forest ecoregions. In each ecoregion, there is clear agreement between the seasonality of EWT and backscatter. This indicates that backscatter is influenced by moisture availability in terms of total terrestrial water storage, which includes groundwater storage. It is noteworthy that this temporal consistency between backscatter and EWT is apparent for both forest (fC in Fig. 4 (b)) and the Guianan Savanna (sG in 4 (e)) despite the contrast between almost zero (0.25 dB) variability in backscatter in fC and the 2.5 dB seasonal cycle in sG.

Figure 5 (a) summarizes the mean seasonal cycle in the slope for the ecoregions of interest. The difference between ecoregions is more pronounced than for backscatter. The seasonal cycle for the evergreen forest ecoregions are similar in magnitude but there are minor differences in the timing of the peak. The differences between the savanna regions are more pronounced

than for backscatter. Significant differences can be seen in the mean slope value, as well as the amplitude and timing of the
seasonal cycle of slope values for each ecoregion of interest.

In Fig. 5(b-e), the seasonal cycle of slope in each ecoregion is compared to the corresponding cycles of radiation, specific
humidity and precipitation which drive photosynthetic activity in the region. In the Jurua-Purus moist forests (Fig. 5(b)), the
change is slope is one-tenth that observed in the other ecoregions. The variations in radiation and specific humidity are also
very limited. Nonetheless, the seasonal cycle of the slope follows that of the radiation with a lag of about 30 days. This can
be explained by the fact that the vegetation phenology in this tropical evergreen forest is driven by radiation (Romatschke and
Houze Jr, 2013). The photosynthetic capacity depends on the available solar energy (Borchert et al., 2015). Energy availability
drives transpiration and the accumulation of leafy biomass. This increases volume scattering from the canopy and therefore
leads to an increase in the slope. Similar results were observed for the other forest ecoregions. In the Marajo varzea flooded
forest (Fig. 5(c)), the variation in slope is much larger, and the seasonal cycle is clearly out of phase with that of the radiation.
The seasonal variations in slope in this ecoregion are dominated by the influence of surface flooding rather than vegetation
water content variations (Sect. 3.1.2).

In the Cerrado (Fig. 5(d)), there is a significant variation in specific humidity, and radiation as well as a strong seasonal
cycle in precipitation. The peak in slope occurs during the driest time of year, when radiation is at a maximum and specific
humidity and precipitation are at a minimum. Recall from Fig. 4, that this is also during the minimum EWT and backscatter
period. Section 3.1.1 provides a detailed analysis of the vegetation types within the Cerrado ecoregion to better understand
these variations. The slope values in the Guianan Savanna (Fig. 5(e)) are the lowest observed in all ecoregions, and also have
the smallest variations among the non-forest cover types. This is consistent with the relatively low, but stable vegetation density
associated with grasslands (Steele-Dunne et al., 2019). In the Beni Savanna (Fig. 5(f)), on the other hand, slope varies as much
as in the Cerrado, and there is a very clear relationship between the slope and the atmospheric forcing data (Fig. 5 (f)). The
maximum slope occurs at the peak of precipitation, EWT (from Fig. 4) and humidity. The minimum slope occurs during the dry
season at the minimum in precipitation, humidity and EWT. This is consistent with the interpretation of slope as an indicator
of vegetation density as the vegetation cover in this savanna changes dramatically in response to atmospheric forcing. The
contrast in the seasonal cycles in slope in Fig. 5 reflect the diversity of the vegetation cover types in the ecoregions and their
varied response to moisture supply and demand.

Figure 6 (a) shows the mean seasonal cycles in curvature for the regions of interest. The differences in the amplitudes of the
seasonal cycles vary considerably among the regions. While the evergreen forests vary less than 0.0005 dB/deg^2, variations
in the wetland regions (Beni savanna and Marajó várzea) are an order of magnitude larger. Aside from the Guianan savanna,
the timing of the seasonal cycle is similar across all ecoregions. Previous research has suggested that curvature is related to
vegetation phenology and structure (Steele-Dunne et al., 2019). Since the vegetation phenology in much of the forested region is
radiation-driven, we hypothesize that the curvature seasonality is related to the radiation and evaporative demand. Wagner et al.
(2016) observed that litterfall coincides with maximum evaporative demand, which would coincide with lower humidity and
higher solar radiation. Leaf flushing is induced by an increase in radiation (Borchert et al., 2015). Figures 6 (b-f) demonstrate
that higher values of curvature generally correspond to lower humidity, higher solar radiation and lower precipitation. It is also
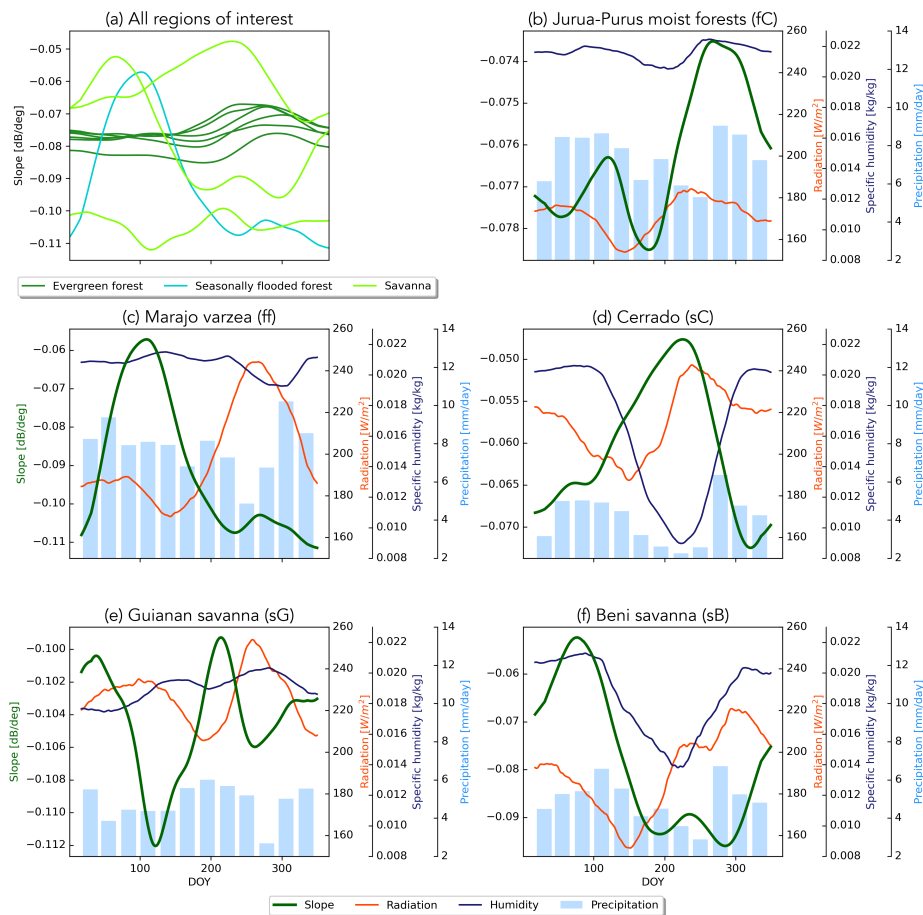
Figure 5. Climatology of slope (green line), radiation (red line), humidity (blue line) and precipitation (bars) for different cover types.

noteworthy that the curvature values in the Guianan savanna (Fig. 6 (e) are positive for much of the year, consistent with the
dominance of grass cover in this region.

3.1.1 Cerrado

Figure 7 provides a detailed map of the Copernicus Global Land Service Land Cover within the Cerrado region Buchhorn
et al. (2020). The dominant cover types are herbaceous cover and shrubland, with patches of cropland and forest. Figures 8 and
9 show the spatial patterns and boxplot per land cover type of mean, maximum and the DOY of the maximum for backscatter,
slope and curvature. The mean backscatter varies between -13 and -7 dB and is highest for forest regions and lowest for
croplands. The DOY for the maximum backscatter varies with latitude, from December to January in the southern region
to April in the northern region. The highest backscatter corresponds with the months of highest precipitation and EWT, the
minimum in backscatter corresponds with the months of lowest moisture availability (Fig. 4). The slope mean and maximum
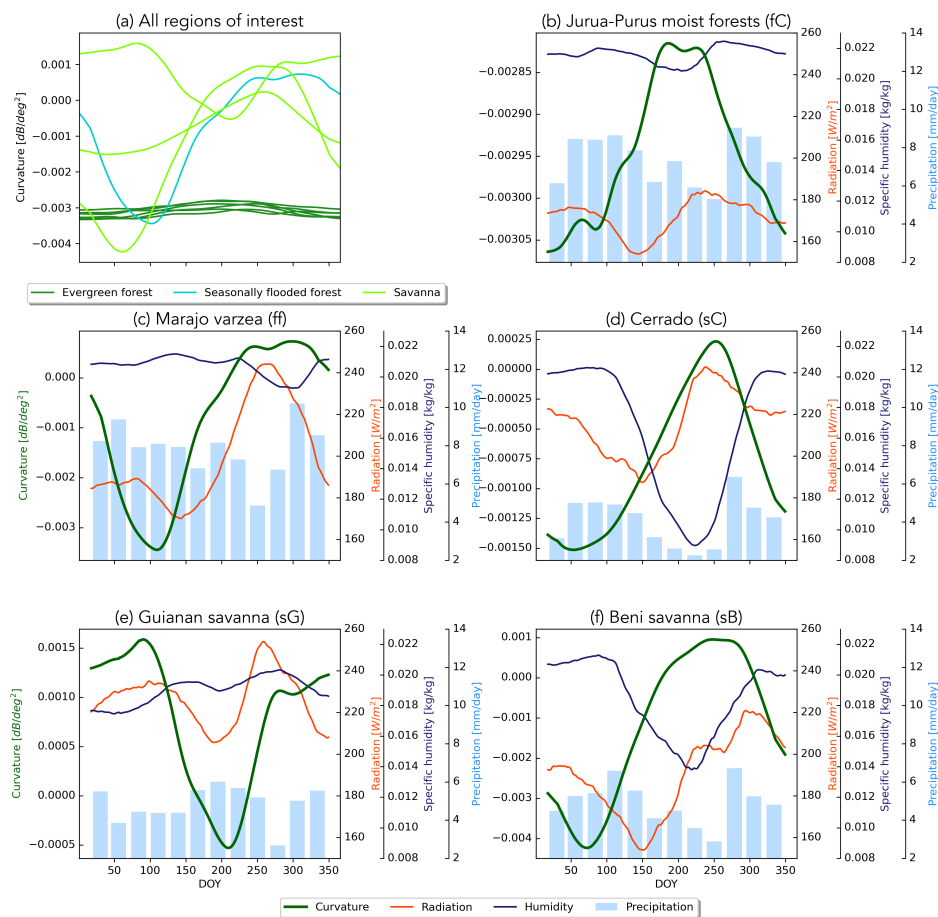
Figure 6. Climatology of curvature (green line), radiation (red line), humidity (blue line) and precipitation (bars) for evergreen forests.

values show a decrease from shrubs to herbaceous to cropland, decreasing with vegetation density. Forests are characterised by high mean and maximum slope values. The seasonal dynamics and DOY of the maximum slope vary strongly with land cover type. In croplands, the maximum of slope occurs between DOY 340-150, corresponding to the highest precipitation and EWT. In natural vegetation, such as herbaceous cover, shrubs and forests, the highest slope occurs between day 200 and 300 and coincides with the minimum in precipitation and EWT and maximum radiation (Fig. 5). Within the Cerrado region, vegetation can be moisture limited or energy limited (Nemani et al., 2003), depending on location and land cover type. Figure 10 shows the slope and radiation dynamics for different land cover classes. To exclude confounding effects due to heterogeneous land cover within ASCAT pixels, we used only pixels with a dominant land cover fraction of > 80%. The slope dynamics in cropland are following the precipitation dynamics and have their peak during the wet season. Herbaceous cover shows two peaks in slope, one coinciding with the wet season at the beginning of the year, and a higher peak coinciding with the dry season and maximum in radiation. The increase in slope coincides with the onset of the increase in radiation. In shrubs and forests, slope
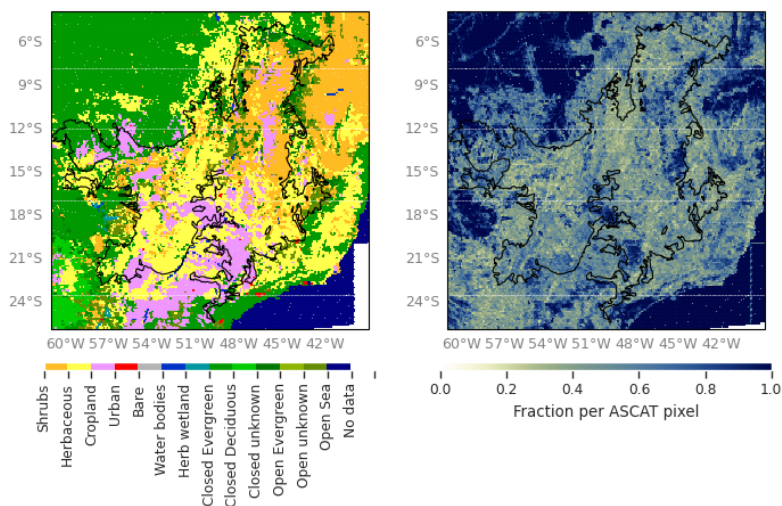
Figure 7. Dominant land cover type (left) and fraction (right) derived from the Copernicus Global Land Service Land Cover (2015) for the Cerrado region Buchhorn et al. (2020)

245   starts to increase after the wet season, but before the increase in radiation (Fig. 10). Shrubs and forests have deeper root systems

246   they can tap into deeper water reservoirs. This enables them to increase photosynthesis and leaf development slightly before

247   or at the onset of increasing radiation even though precipitation is at its minimum. Chave et al. (2010) found that, among the

248   tropical forest types in South America, the highest seasonality in litterfall was observed in "low" stature forests, such as those

249   found in the Cerrado. They also cite Wright and Van Schaik (1994) to argue that seasonality of solar radiation rather than

250   precipitation may the most important trigger for leaf flushing and leaf abcission. Croplands and herbaceous vegetation show

251   positive curvatures, whereas forests are characterised by negative curvatures with the maximum values occurring between DOY

252   200 and 300 across the Cerrado. The positive curvature for crops and herbaceous vegetation can be explained by the vertical

253   structure of the vegetation.

254   **3.1.2 Seasonal Flooding**

255   Fig. 11 shows the striking effect of seasonal flooding on the incidence angle dependence of backscatter. This relationship was

256   obtained using Equation 1 for a reference angle of $40°$ with the climatological mean values of σ_{40}°, slope and curvature for

257   several days during the year. The flooded period is indicated in shades of blue. First, note that σ_{40}° is around 2 dB higher during

258   the seasonal flooding. This is due to multiple scattering between the water surface and the vegetation. Recall from Fig. 5 that

259   the slope is slightly higher during this period as this multiple scattering is apparently slightly less sensitive to incidence angle

260   than scattering from the vegetation during non-flooded period. However, the most noteworthy difference is in the curvature. In
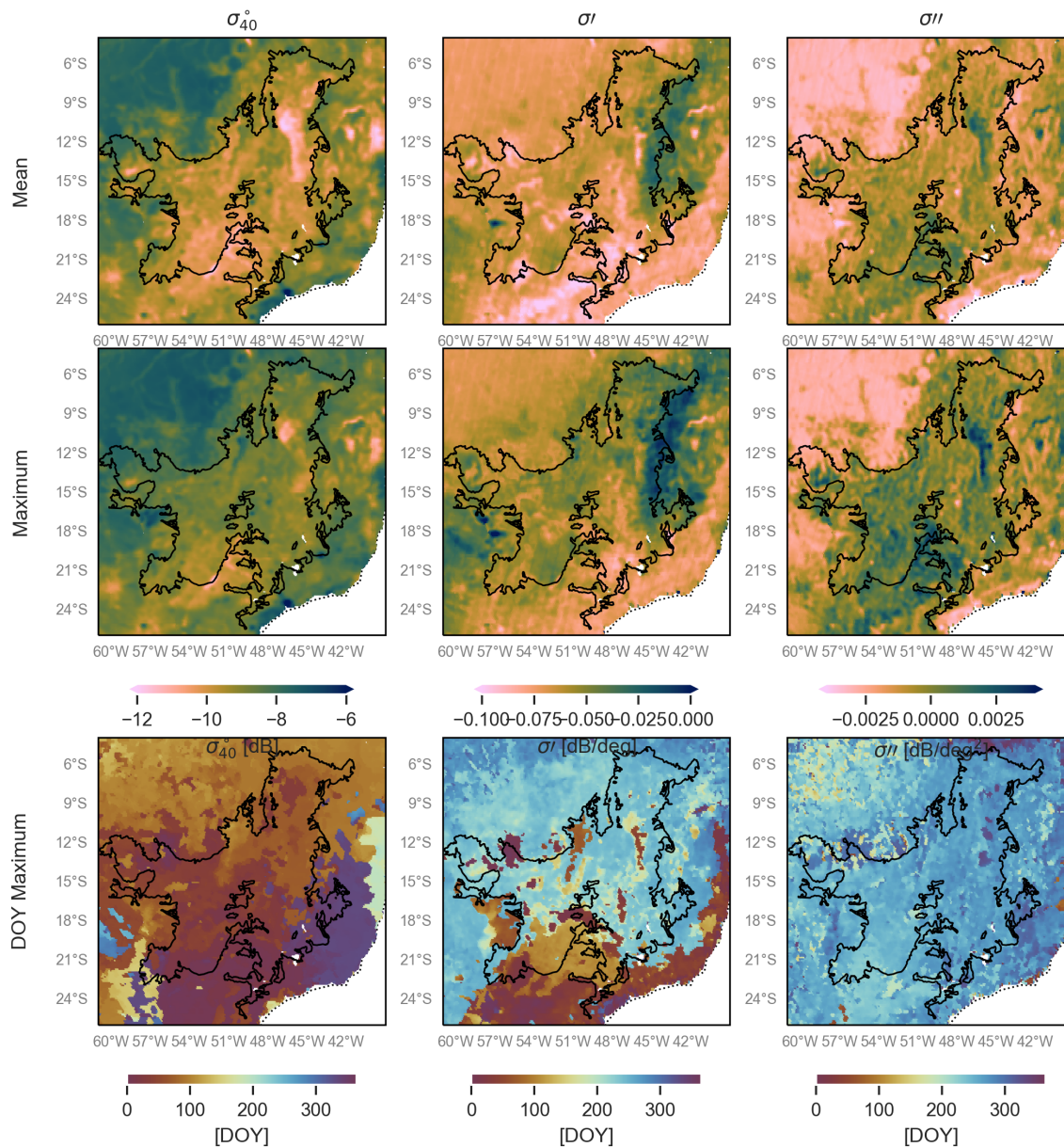
Figure 8. Mean, maximum and day of year of maximum for backscatter, slope and curvature over the Cerrado.
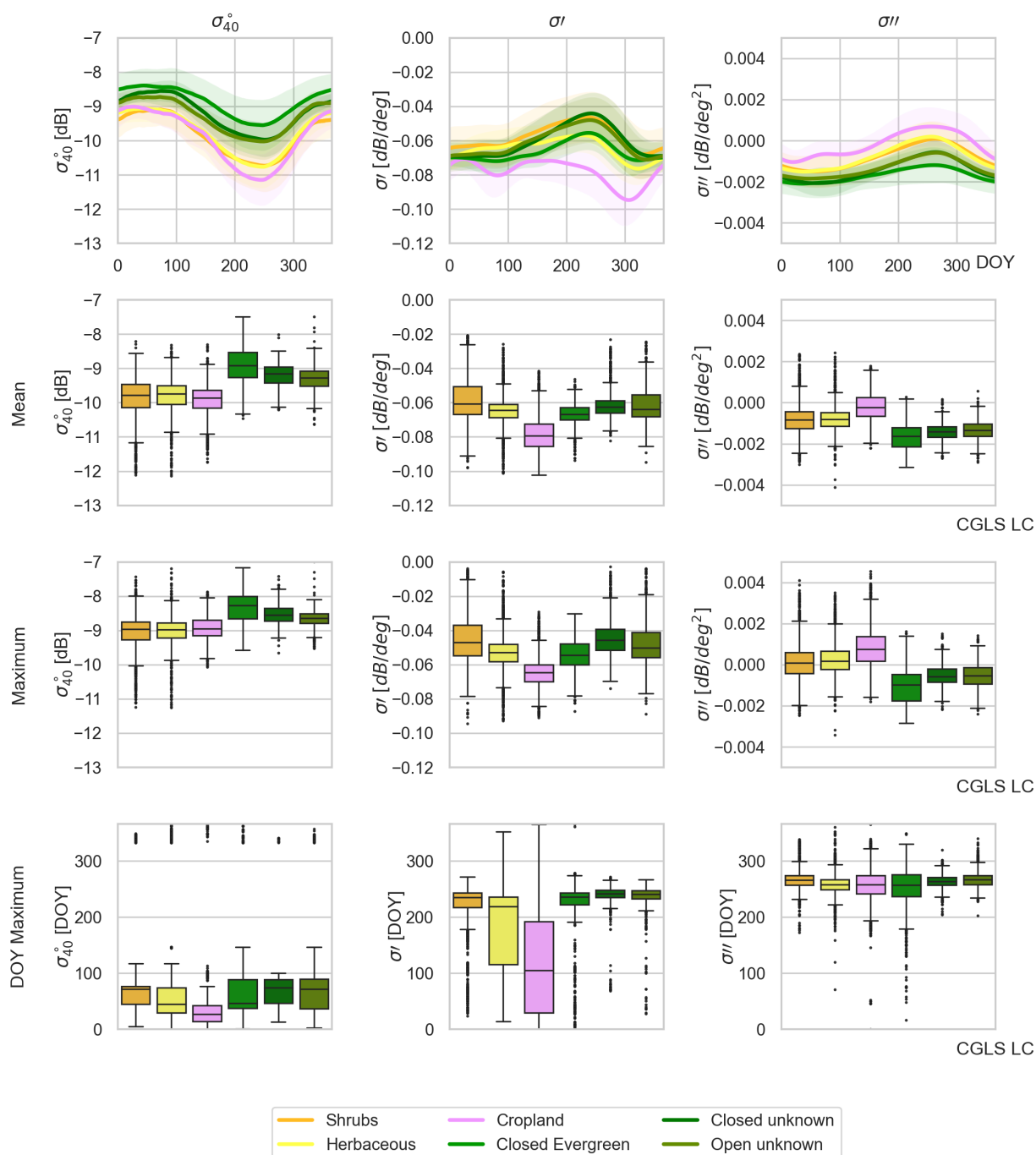
Figure 9. Time series averaged per land cover class and boxplots of mean, maximum and day of year of maximum for backscatter, slope and curvature over the Cerrado.
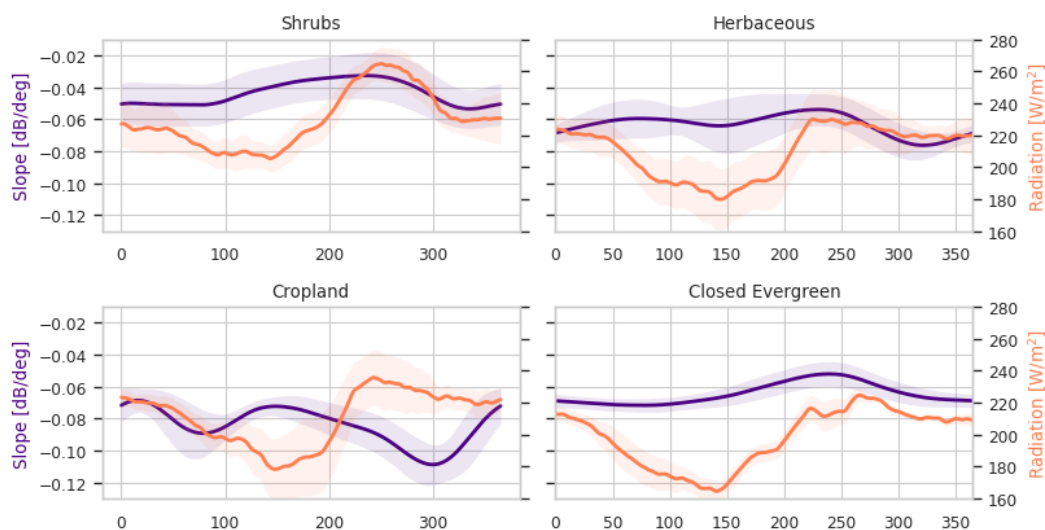
Figure 10. Seasonal cycle of slope and radiation per land cover class in the Cerrado region. Only ASCAT pixels in which the fraction of the dominant land cover type exceeds 80% are included.
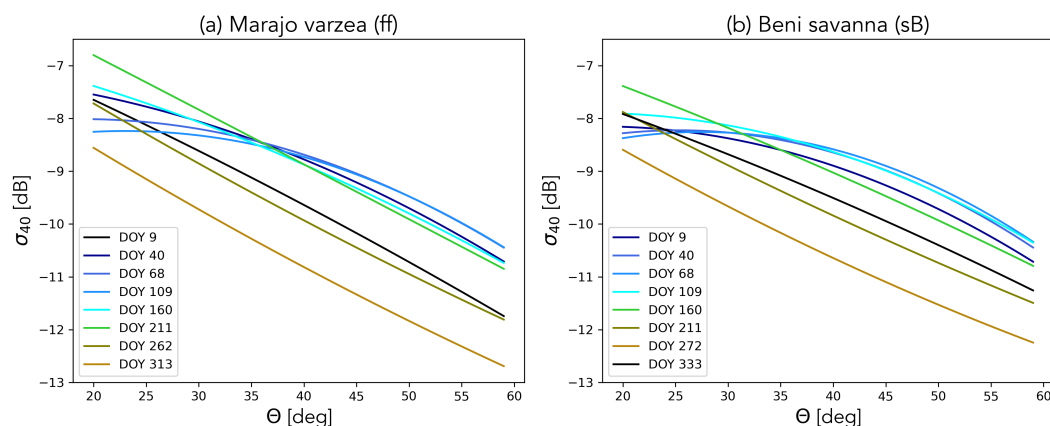
Figure 11. Averaged backscatter as a function of incidence angle for several dates in the Marajo varzea (a) and Beni Savanna (b) ecoregions.

261 both ecoregions, the curvature changes considerably and even changes sign during the flooded period. This illustrates that the

262 curvature includes useful information on changes in the scattering mechanisms, which are related to physical changes at the

263 land surface.
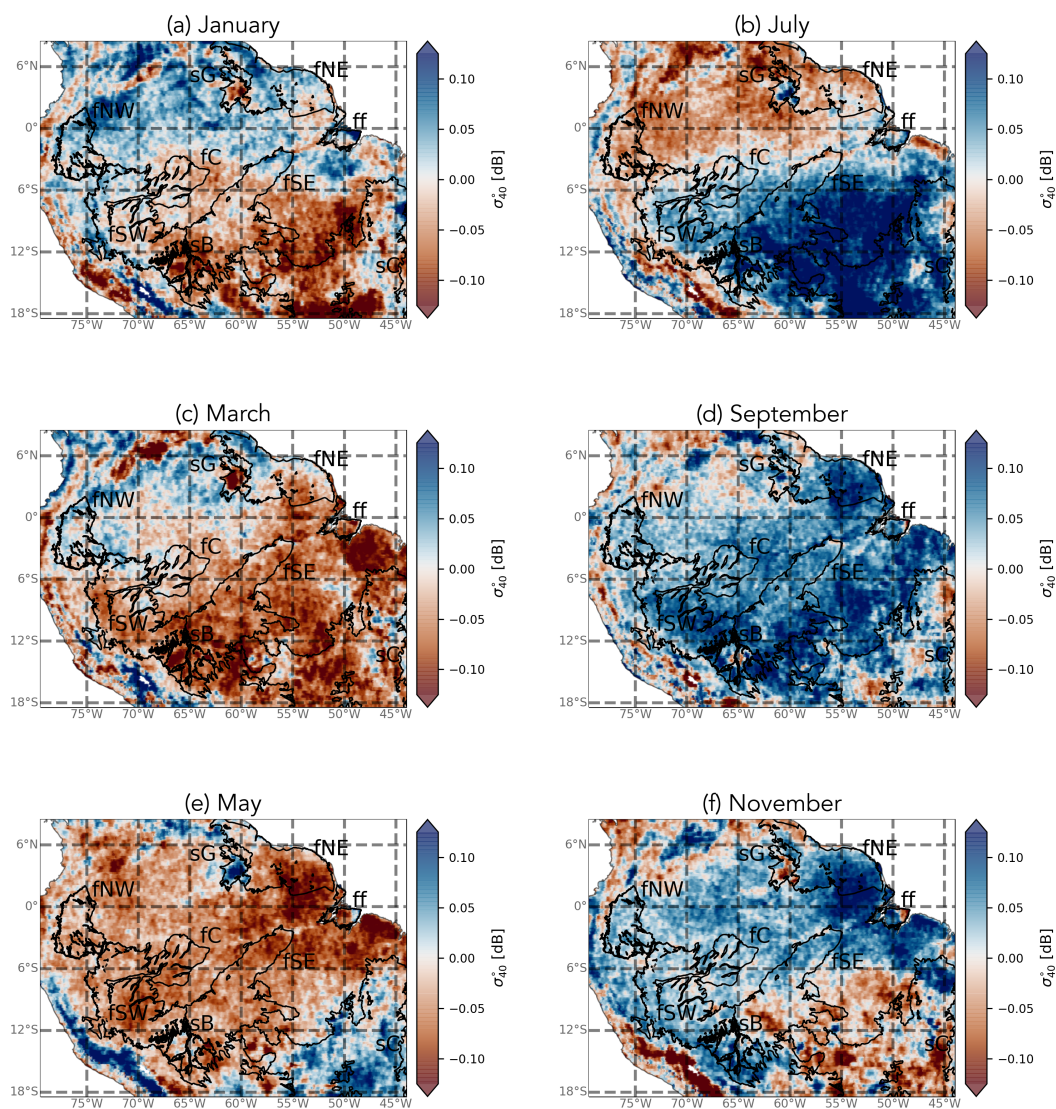
Figure 12. Map of monthly mean diurnal differences in sig_{40} (morning minus evening passes) for different months in the year.

3.2 Diurnal Differences

Figure 12 shows the mean diurnal differences for backscatter in the study area for alternate months in the year, where positive values indicate that values are higher during the descending (10 am) overpass than those from the ascending (10 pm) overpass. The diurnal differences in backscatter are generally very small, with maximum values less than 0.15 dB. Nonetheless, there is a clear seasonal variation, broadly following that of EWT (shown in Fig. 13).
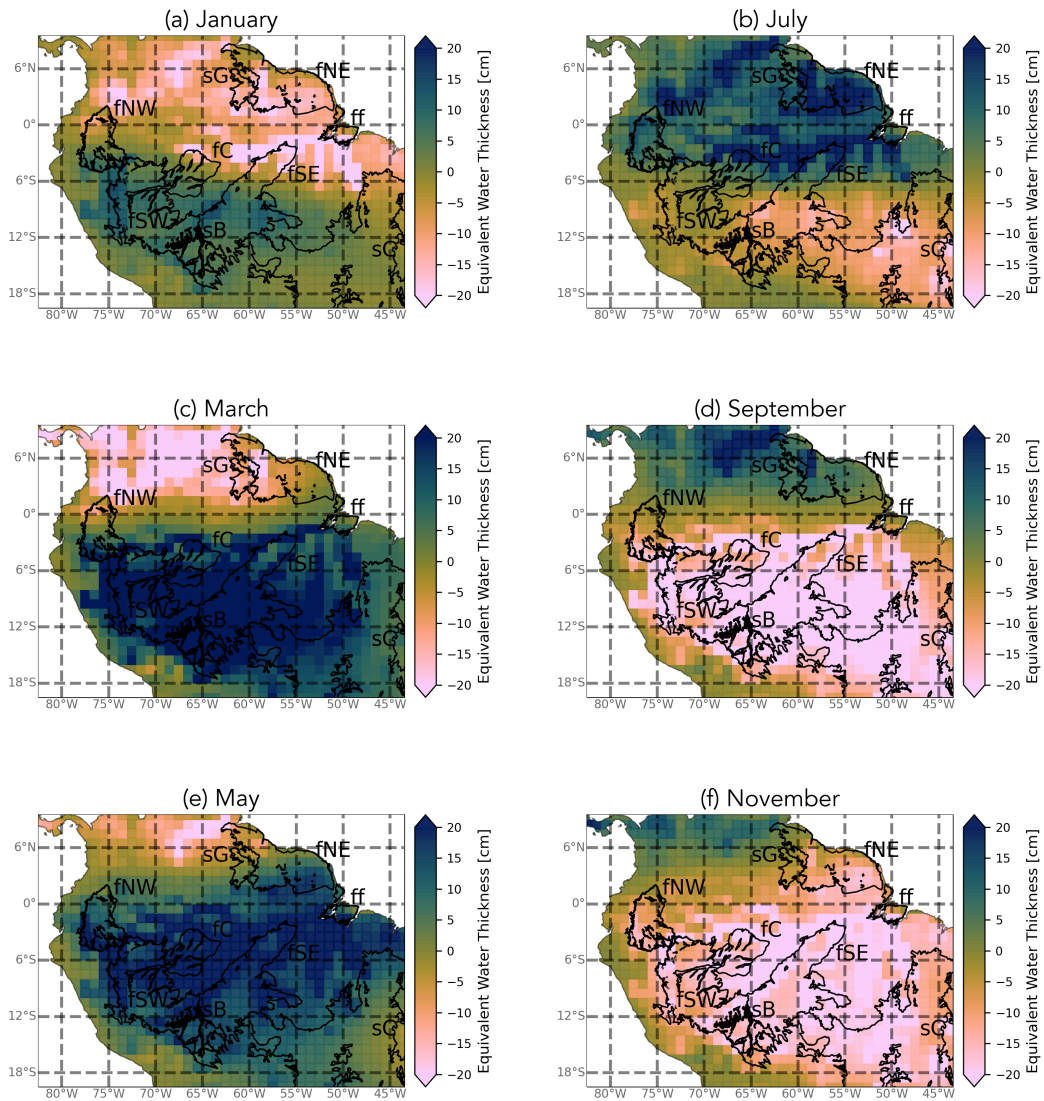
Figure 13. Map of monthly mean Equivalent Water Thickness from GRACE

269   For most of the domain, especially the evergreen forests, high values in EWT coincide with negative diurnal differences in

270   backscatter and vice versa. During periods of maximum EWT, the backscatter is higher in the evening than in the morning.

271   This is consistent with the finding that precipitation in tropical South America (since it is generally produced by convective

272   systems) predominantly occurs in the late afternoons and evenings (Romatschke and Houze Jr, 2013). Hence, these higher

273   backscatter values are due to the canopy being wetter in the evening.

274   During the drier periods (e.g. September (e) and November (f) in the south of the study area), backscatter is higher at 10 am

275   than at 10 pm, consistent with the loss of moisture through transpiration during the day. In a light-limited evergreen forest

276   such as the Amazon (rather than a water-limited forest), the canopy photosynthetic capacity seasonality is driven by radiation

277   (Wagner et al., 2016). When the plants are phenologically active, they lose water during the daytime through transpiration

278   resulting in lower evening backscatter values. The results in Fig. 12 and 13 are consistent with the findings of previous studies

279   by Frolking et al. (2011) and Friesen et al. (2012) who also found the morning backscatter over Amazonia to be higher (on

280   average) than the evening values due to higher water content in the vegetation. In the areas surrounding the evergreen forests,

281   the patterns can be less straight-forward. Note, for example, that the diurnal difference in σ°_{40} in the Guianan savanna (sG)

282   consistently has the opposite sign to that of the surrounding forest.

283   In Fig. 14, the seasonal cycle of the diurnal difference in σ°_{40} is compared to those of the radiation, precipitation and EWT

284   for each of the ecoregions of interest. Figure 14(a) is indicative of the seasonal variations observed across the evergreen forest

285   ecoregions. Note that the diurnal differences are very small (< 0.06 dB). Recall from Fig. 4, 5 and 6 that the backscatter, slope

286   and curvature in these evergreen forests was essentially stable throughout the year, so even this small diurnal difference is

287   noteworthy given the limited seasonal variation. As mentioned in the discussion of Fig. 12, evening values are higher than

288   morning values during the EWT maximum and vice versa. Diurnal differences are larger in the Marajo varzea (Fig. 14(b)), but

289   interpreting their seasonal variation is complicated by the seasonal inundation. In the Cerrado and Beni Savanna ecoregions

290   (Fig. 14(c) and (e)), the diurnal differences in backscatter are almost twice as large as those observed in the evergreen forest

291   regions. Morning values are up to 0.1 dB higher than evening values during the dry season due to loss of plant moisture during

292   the day. Similar to the forest regions, evening backscatter values are higher during the rainy season. The Guianan savanna is

293   quite distinct in that morning backscatter is up to 0.15 dB higher than evening backscatter during the EWT and backscatter

294   peak. One possible explanation for this unusual seasonal cycle is that it is related to a change in the relative dominance of the

295   forests and grasslands in the backscatter signal. The transition from positive to negative curvature values during the EWT peak

296   indicate an increased contribution from tree patches and shrubs during the wetter period. The higher backscatter in the morning

297   may be due to water uptake in the trees during the night.

3.3   The 2010 and 2015 droughts

299   During the study period (2007-16), two major droughts occurred in Amazonia, in 2010 and 2015. Figure 15 shows the spatial

300   distribution of anomalies in σ°_{40}, slope and curvature during the peak of the droughts from June to September 2010 and October

301   to December 2015. Two regions of interest are indicated in the maps, the savanna Cerrado (sC) ecoregion and Southwest

302   Amazon moist forests (fsW). The 2010 drought was most severe over southern and western Amazonia (Panisset et al., 2018).
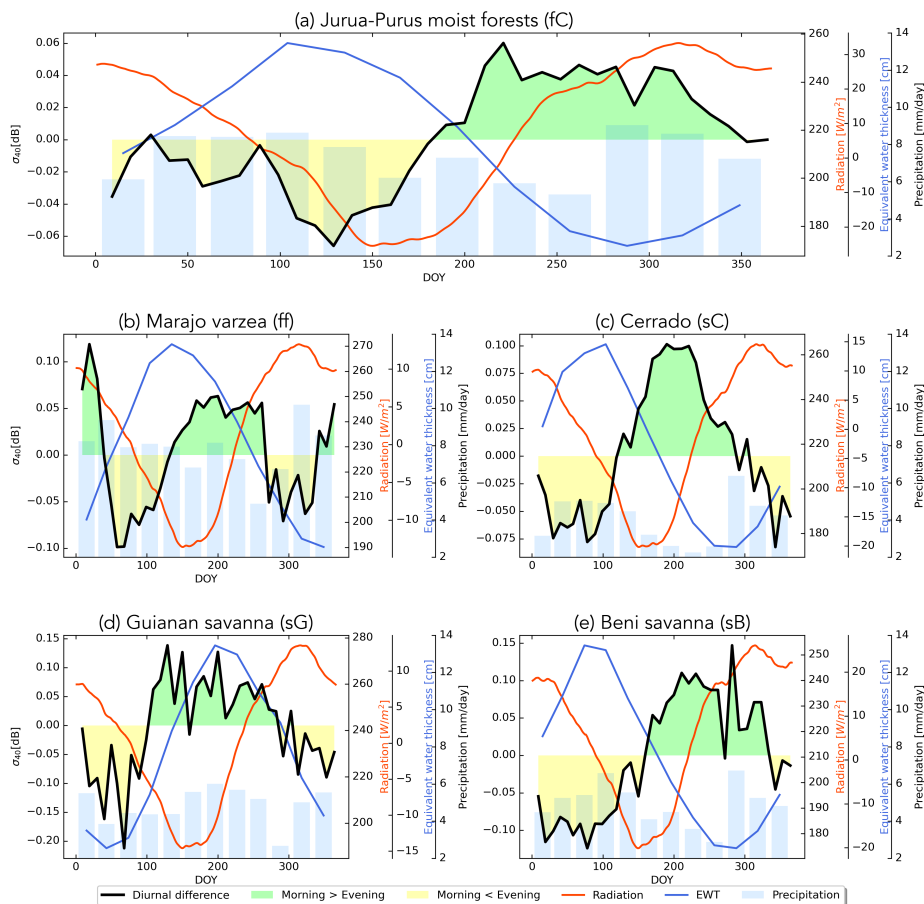
Figure 14. Seasonal cycle of diurnal difference in backscatter (black line), radiation (red line), EWT (blue line), and precipitation (bars) for different cover typres. Green (yellow) fill indicates days in which backscatter is higher (lower) in the morning than in the evening.

303   The 2015 drought was considered a "record-breaking" event with stronger warming than that seen in previous events (Jiménez-
304   Muñoz et al., 2016). According to Panisset et al. (2018), there was a "pronounced lack of rainfall availability during late spring
305   and early summer". The 2015 drought was more widespread than the event in 2010, and strongest in eastern Amazonia.

306   Negative anomalies are observed in σ_{40}°, especially in the southern regions and in the Cerrado in 2010 and in eastern regions
307   in 2015. Note that the most eastern part of the Cerrado shows positive anomalies in 2010. The forests in fsW show minor
308   negative anomalies (<0.1 dB) in σ_{40}° in 2010 and slightly stronger negative anomalies in 2015. Negative anomalies in backscat-
309   ter from QSCAT were also observed during the 2005 drought (Saatchi et al. (2013); Frolking et al. (2017)). The slope and
310   curvature do not show clear spatial patterns in anomalies during the 2010 drought, although the southern region shows slightly
311   more positive anomalies. A clear positive anomaly can be observed in the slope in eastern Amazonia in the 2015 drought. The
312   curvature shows less clear patterns, although a striping pattern can be seen, likely related to swaths.

313   Figure 16 shows the time series of anomalies in backscatter, slope and curvature for the moist forests in fsW and the Cerrado

314   region for the 2010 and 2015 drought. The backscatter, slope and curvature over the closed evergreen forest in fsW shows very

315   little variation (both in time and space) during both droughts. A slight increase up to 0.002 in slope can be observed during

316   the peak of the 2015 drought. This demonstrates that the fsW forests are stable for satellite calibration. The Cerrado shows

317   varying responses depending on land cover type and are therefore investigated further. Negative anomalies in σ_{40}° in cropland

318   and herbaceous land cover can be seen during both droughts. Especially during the 2010 drought the croplands in the Cerrado

319   are strongly affected, with a negative anomaly of >-1dB for some pixels. During the more extensive drought in 2015, σ_{40}° in

320   forest is also affected and negative anomalies up to -1.5 dB are observed. The slope shows minor positive anomalies during

321   the peak of the drought in 2010. In an analysis of drought impact on VOD over the forests in southern Amazonia, Liu et al.

322   observed similar positive anomalies in VOD from May to August during the 2010 drought. Negative anomalies in VOD were

323   only observed during later stages of the drought, from August to October. In 2010, negative slope anomalies in the Cerrado

324   are observed from October on. During the 2015 drought strong positive anomalies in slope and curvature are present over the

325   Cerrado especially in forests. Contrary to the drought of 2010, the peak of the 2015 drought occurs during the precipitation

326   season in the Cerrado. Normally the precipitation season is characterised by lower radiation, and the positive anomalies in

327   radiation during the drought might enhance vegetation growth.

328   **4   Conclusions**

329   In this study, ASCAT backscatter, slope and curvature were analyzed in conjunction with meteorological data and terrestrial

330   water storage from GRACE in the Amazon region. Previous results, limited to grasslands, had suggested that the slope and

331   curvature contained useful information for monitoring vegetation water dynamics. However, the current study is the first to

332   relate the spatial and temporal variations in slope and curvature to moisture availability and demand. Furthermore, it confirms

333   that the conclusions of Steele-Dunne et al. (2019) can be extended to a wide range of cover types.

334   Results show that the unique viewing geometry of ASCAT provides valuable insight into vegetation water dynamics across a

335   diverse range of ecoregions. Strong temporal consistency was found between ASCAT backscatter and GRACE EWT, with the

336   maximum backscatter coinciding with periods of maximum moisture availability. Spatial patterns in mean and range of slope

337   reflected spatial patterns in vegetation density. The seasonal cycle in slope was found to follow the moisture availability and

338   demand indicated by meteorological data and their influence on phenology. A detailed analysis per land cover type over the

339   Cerrado demonstrated this. Slope dynamics were concurrent with precipitation in croplands and herbaceous cover, although

340   herbaceous cover showed a second peak coinciding with the maximum in radiation. Slope dynamics in shrubs and forest

341   corresponded with radiation, although the onset in increasing slope preceded the onset of increasing radiation. This may be due

342   to leaf flushing, but it is difficult to draw a firmer conclusion given the limited availability of ground data Chave et al. (2010).

343   While the mechanism driving these variations in slope may not be immediately clear, it is important to note that there are open

344   questions around the process of litterfall and its relation to precipitation and radiation in general. A recent study from Hashimoto

345   et al. (2021) demonstrated that the temporal density of optical data from the Advanced Baseline Imager (ABI) onboard the
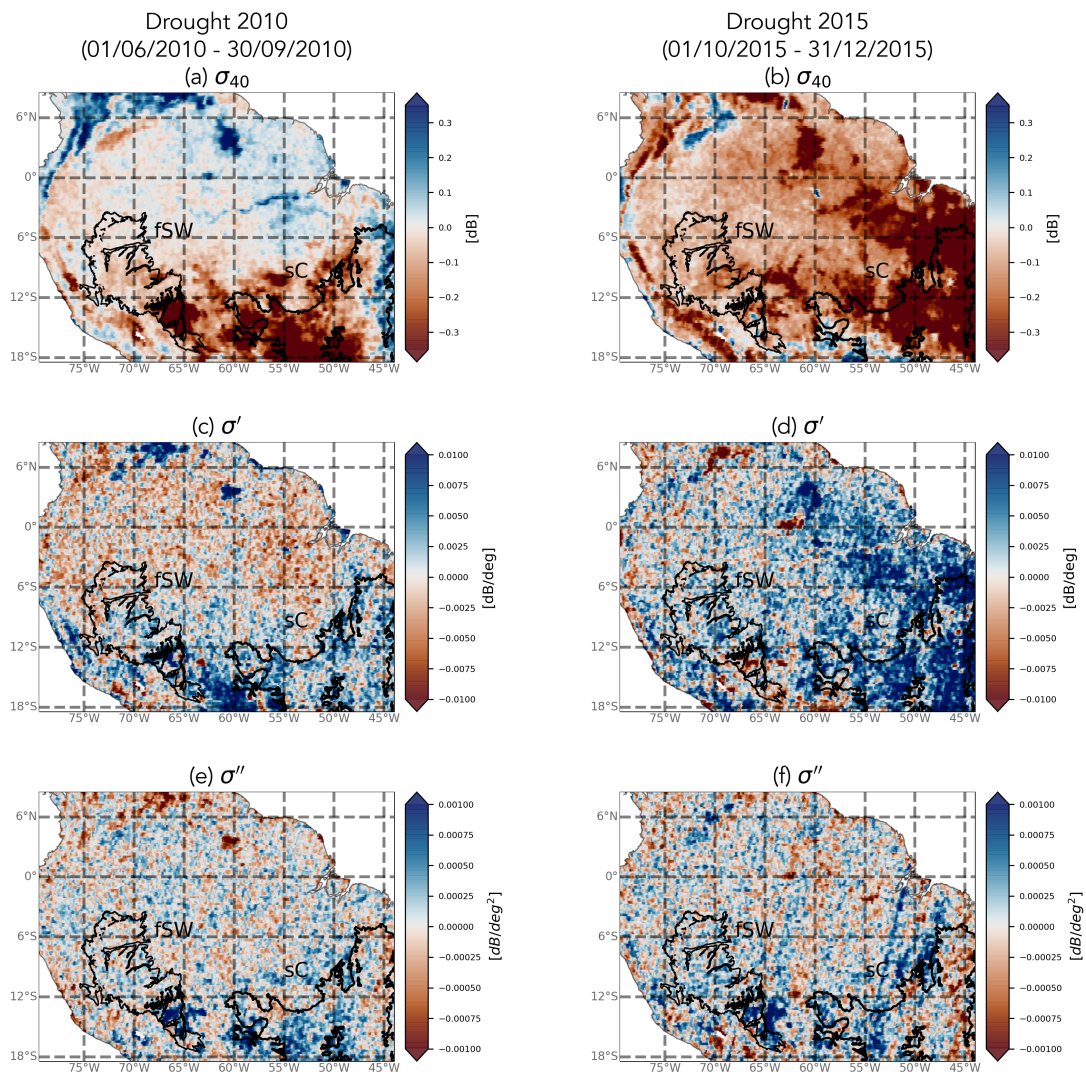
Figure 15. Spatial patterns in anomalies in backscatter, slope and curvature in response to the 2010 and 2015 droughts.
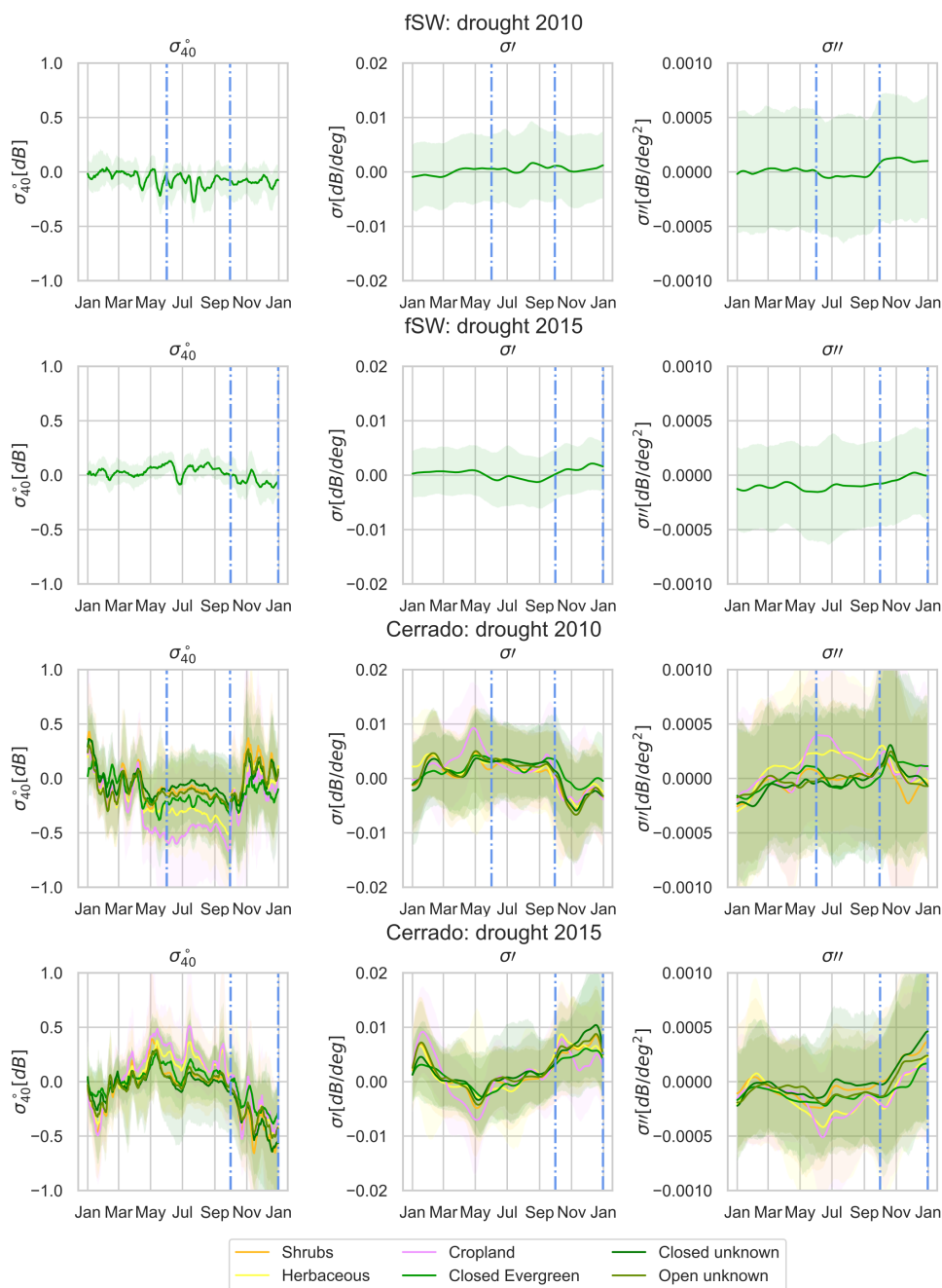
Figure 16. Time series of anomalies in backscatter, slope and curvature for moist forest (fsW) and Cerrado region. The shaded areas indicate the 5th and 95th percentile. The peak drought intervals (June-September 2010 and September-December 2015) are shown within dotted blue lines.

346 Geostationary Operational Environmental Satellite 16 (GOES-16) yields unprecedented detail on the seasonality of NDVI
347 and LAI in the evergreen Amazon forests. A comparison of ASCAT slope and curvature and ABI data may yield additional
348 insight into the connection between slope, curvature and litterfall in the various ecoregions of our study area. Consistent
349 with the findings of Steele-Dunne et al. (2019) in a study limited to grasslands, variations in curvature seem to be related to
350 phenological change. Temporal consistency between the curvature and meteorological data suggests sensitivity to events such
351 as litterfall and leaf flushing. Areas affected by seasonal flooding exhibited dramatic changes in both backscatter and curvature
352 due to a suspected increase in multiple scattering between water on the surface and the vegetation.

353 Diurnal variations (i.e. the difference between morning and evening overpasses) were generally small, particularly in the
354 evergreen forests. Nonetheless, their relation to the timing of precipitation highlights the importance of overpass time in using
355 microwave observations for vegetation monitoring. Diurnal differences in backscatter during the dry season are dominated by
356 transpiration losses. Long-term monitoring of these diurnal differences could provide insight into moisture availability and
357 its influence on transpiration and vegetation functioning. Consistent with previous studies on the effect of drought on the
358 backscatter signal over the Amazon forests (Frolking et al., 2011; Saatchi et al., 2013), a negative anomaly in backscatter was
359 observed during the 2010 and 2015 drought, although this was minor for the moist forests, strong anomalies were observed in
360 the Cerrado. The slope showed positive anomalies during the drought events in the Cerrado, similar to positive anomalies in
361 VOD over forests observed by Liu et al. who attributed this to enhanced canopy growth due to increased radiation. Persistent
362 positive anomalies in radiation were observed over the Cerrado, especially in 2015. The analysis confirms the confounding
363 effects of mechanisms driving variation in slope in these regions and further research is needed.

364 This improved understanding of slope and curvature is valuable in terms of our ability to use ASCAT for vegetation mon-
365 itoring, and specifically for vegetation water dynamics. The slope and curvature are used to produce the vegetation optical
366 depth from ASCAT (Vreugdenhil et al., 2016). Improved understanding of the slope and curvature and how they are affected
367 by vegetation structure and water content, and interactions between the soil and vegetation is essential to improve our ability
368 to interpret and optimally use VOD derived from ASCAT. Furthermore, the fact that the slope and curvature themselves reveal
369 different aspects of the vegetation response to the balance between moisture availability and demand means they are potentially
370 useful low-level observables, i.e. they are obtained with minimal processing, and avoid the assumptions and simplifications re-
371 quired to retrieve geophysical variables. The results of this study suggest that their information content can be directly exploited
372 to monitor vegetation water dynamics.

373 *Author contributions.* AP, SSD and MV were responsible for the conceptualization, methodology, formal analysis, investigation, visual-
374 ization and writing (original draft preparation). SH provided resources (ASCAT data). RO contributed to the investigation. SSD and MV
375 provided supervision. All authors contributed to writing (review and editing).

376 *Competing interests.* The authors declare that no competing interests are present.

377 *Acknowledgements.* Susan Steele-Dunne was supported by Vidi Grant 14126 from The Netherlands Organization for Scientific Research

378 (NWO). Mariette Vreugdenhil was supported by ESA's Living Planet Fellowship SHRED (contract number 4000125441/18/I-NS).

References

Attema, E. P.: The active microwave instrument on-board the ERS-1 satellite, Proceedings of the IEEE, 79, 791–799, publisher: IEEE, 1991.

Birrer, I., Bracalente, E., Dome, G., Sweet, J., and Berthold, G.: σ signature of the Amazon rain forest obtained from the SeaSat scatterometer, IEEE Transactions on Geoscience and Remote Sensing, GE-20, 11–17, 1982.

Borchert, R., Calle, Z., Strahler, A. H., Baertschi, A., Magill, R. E., Broadhead, J. S., Kamau, J., Njoroge, J., and Muthuri, C.: Insolation and photoperiodic control of tree development near the equator, New Phytologist, 205, 7–13, 2015.

Bradley, A. V., Gerard, F. F., Barbier, N., Weedon, G. P., Anderson, L. O., Huntingford, C., Aragão, L. E., Zelazowski, P., and Arai, E.: Relationships between phenology, radiation and precipitation in the Amazon region, Global Change Biology, 17, 2245–2260, 2011.

Buchhorn, M., Smets, B., Bertels, L., Roo, B. D., Lesiv, M., Tsendbazar, N.-E., Herold, M., and Fritz, S.: Copernicus Global Land Service: Land Cover 100m: collection 3: epoch 2015: Globe, https://doi.org/10.5281/zenodo.3939038, type: dataset, 2020.

Camarão, A., Júnior, L., Dutra, S., et al.: Flooded pasture production for grazing buffalo in the brazilian Amazon region., in: Embrapa Amazônia Oriental-Artigo em anais de congresso (ALICE), pp. 68–82, In: Buffalo Symposium Of Americas, 1., 2002, Belém. Proceedings of the . . . , 2002.

Chaparro, D., Duveiller, G., Piles, M., Cescatti, A., Vall-llossera, M., Camps, A., and Entekhabi, D.: Sensitivity of L-band vegetation optical depth to carbon stocks in tropical forests: a comparison to higher frequencies and optical indices, Remote Sensing of Environment, 232, 111 303, https://doi.org/10.1016/j.rse.2019.111303, 2019.

Chave, J., Navarrete, D., Almeida, S., Álvarez, E., Aragão, L. E. O. C., Bonal, D., Châtelet, P., Silva-Espejo, J. E., Goret, J.-Y., von Hildebrand, P., Jiménez, E., Patiño, S., Peñuela, M. C., Phillips, O. L., Stevenson, P., and Malhi, Y.: Regional and seasonal patterns of litterfall in tropical South America, Biogeosciences, 7, 43–55, https://doi.org/10.5194/bg-7-43-2010, publisher: Copernicus GmbH, 2010.

De Jeu, R. A.: Retrieval of land surface parameters using passive microwave remote sensing, PhD diss., Vrije Universiteit Amsterdam, 2003.

Eiten, G.: The cerrado vegetation of Brazil, The Botanical Review, 38, 201–341, 1972.

Fernandez-Moran, R., Al-Yaari, A., Mialon, A., Mahmoodi, A., Al Bitar, A., De Lannoy, G., Rodriguez-Fernandez, N., Lopez-Baeza, E., Kerr, Y., and Wigneron, J.-P.: SMOS-IC: An Alternative SMOS Soil Moisture and Vegetation Optical Depth Product, Remote Sensing, 9, 457, https://doi.org/10.3390/rs9050457, 2017.

Figa-Saldaña, J., Wilson, J. J., Attema, E., Gelsthorpe, R., Drinkwater, M. R., and Stoffelen, A.: The advanced scatterometer (ASCAT) on the meteorological operational (MetOp) platform: A follow on for European wind scatterometers, Canadian Journal of Remote Sensing, 28, 404–412, publisher: Taylor & Francis, 2002.

Forkel, M., Andela, N., Harrison, S. P., Lasslop, G., van Marle, M., Chuvieco, E., Dorigo, W., Forrest, M., Hantson, S., Heil, A., Li, F., Melton, J., Sitch, S., Yue, C., and Arneth, A.: Emergent relationships with respect to burned area in global satellite observations and fire-enabled vegetation models, Biogeosciences, 16, 57–76, https://doi.org/10.5194/bg-16-57-2019, publisher: Copernicus GmbH, 2019.

Friesen, J., Steele-Dunne, S. C., and van de Giesen, N.: Diurnal differences in global ERS scatterometer backscatter observations of the land surface, IEEE Transactions on Geoscience and Remote Sensing, 50, 2595–2602, 2012.

Frison, P. L., Mougin, E., and Hiernaux, P.: Observations and interpretation of seasonal ERS-1 wind scatterometer data over northern Sahel (Mali), Remote Sensing of Environment, 63, 233–242, publisher: Elsevier, 1998.

Frolking, S., Milliman, T., Palace, M., Wisser, D., Lammers, R., and Fahnestock, M.: Tropical forest backscatter anomaly evident in SeaWinds scatterometer morning overpass data during 2005 drought in Amazonia, Remote Sensing of Environment, 115, 897–907, 2011.

415 Frolking, S., Hagen, S., Braswell, B., Milliman, T., Herrick, C., Peterson, S., Roberts, D., Keller, M., and Palace, M.: Evaluating multiple
416   causes of persistent low microwave backscatter from Amazon forests after the 2005 drought, PloS one, 12, e0183 308, 2017.

417 Hahn, S., Reimer, C., Vreugdenhil, M., Melzer, T., and Wagner, W.: Dynamic characterization of the incidence angle dependence of backscat-
418   ter using metop ASCAT, IEEE Journal of Selected Topics in Applied Earth Observations and Remote Sensing, 10, 2348–2359, 2017.

419 Hamilton, S. K., Sippel, S. J., and Melack, J. M.: Seasonal inundation patterns in two large savanna floodplains of South America: the Llanos
420   de Moxos (Bolivia) and the Llanos del Orinoco (Venezuela and Colombia), Hydrological Processes, 18, 2103–2116, 2004.

421 Hashimoto, H., Wang, W., Dungan, J. L., Li, S., Michaelis, A. R., Takenaka, H., Higuchi, A., Myneni, R. B., and Nemani, R. R.: New
422   generation geostationary satellite observations support seasonality in greenness of the Amazon evergreen forests, Nature Communications,
423   12, 684, https://doi.org/10.1038/s41467-021-20994-y, number: 1 Publisher: Nature Publishing Group, 2021.

424 Hordijk, I., Meijer, F., Nissen, E., Boorsma, T., and Poorter, L.: Cattle affect regeneration of the palm species Attalea princeps in a Bolivian
425   forest–savanna mosaic, Biotropica, 51, 28–38, 2019.

426 Huffman, G. J., Adler, R. F., Bolvin, D. T., and Gu, G.: Improving the global precipitation record: GPCP Version 2.1, Geophysical Research
427   Letters, 36, https://doi.org/https://doi.org/10.1029/2009GL040000, 2009.

428 Jarlan, L., Mougin, E., Frison, P. L., Mazzega, P., and Hiernaux, P.: Analysis of ERS wind scatterometer time series over Sahel (Mali),
429   Remote Sensing of Environment, 81, 404–415, https://doi.org/10.1016/S0034-4257(02)00015-9, 2002.

430 Jiménez-Muñoz, J. C., Mattar, C., Barichivich, J., Santamaría-Artigas, A., Takahashi, K., Malhi, Y., Sobrino, J. A., and Van Der Schrier, G.:
431   Record-breaking warming and extreme drought in the Amazon rainforest during the course of El Niño 2015–2016, Scientific reports, 6,
432   33 130, 2016.

433 Konings, A. G., Piles, M., Rötzer, K., McColl, K. A., Chan, S. K., and Entekhabi, D.: Vegetation optical depth and scattering
434   albedo retrieval using time series of dual-polarized L-band radiometer observations, Remote Sensing of Environment, 172, 178–189,
435   https://doi.org/10.1016/j.rse.2015.11.009, 2016.

436 Konings, A. G., Rao, K., and Steele-Dunne, S. C.: Macro to micro: microwave remote sensing of plant water con-
437   tent for physiology and ecology, New Phytologist, 223, 1166–1172, https://doi.org/https://doi.org/10.1111/nph.15808, _eprint:
438   https://nph.onlinelibrary.wiley.com/doi/pdf/10.1111/nph.15808, 2019.

439 Landerer, F. W. and Swenson, S.: Accuracy of scaled GRACE terrestrial water storage estimates, Water resources research, 48, 2012.

440 Liu, Y. Y., de Jeu, R. A., McCabe, M. F., Evans, J. P., and van Dijk, A. I.: Global long-term passive microwave satellite-based retrievals of
441   vegetation optical depth, Geophysical Research Letters, 38, http://onlinelibrary.wiley.com/doi/10.1029/2011GL048684/full, 2011.

442 Liu, Y. Y., Van Dijk, A. I., De Jeu, R. A., Canadell, J. G., McCabe, M. F., Evans, J. P., and Wang, G.: Recent reversal in loss of global
443   terrestrial biomass, Nature Climate Change, 5, 470–474, http://www.nature.com/nclimate/journal/v5/n5/abs/nclimate2581.html, 2015.

444 Liu, Y. Y., van Dijk, A. I., Miralles, D. G., McCabe, M. F., Evans, J. P., de Jeu, R. A., Gentine, P., Huete, A., Parinussa, R. M., Wang, L.,
445   et al.: Enhanced canopy growth precedes senescence in 2005 and 2010 Amazonian droughts, Remote sensing of environment, 211, 26–37,
446   2018.

447 Marengo, J. A., Tomasella, J., Alves, L. M., Soares, W. R., and Rodriguez, D. A.: The drought of 2010 in the context of historical droughts
448   in the Amazon region, Geophysical Research Letters, 38, 2011.

449 Metzler, T.: Vegetation Modelling in WARP 6.0, in: Proc. EUMETSAT Meteorological Satellite Conf., pp. 1–7, Vienna, Austria, 2013.

450 Moesinger, L., Dorigo, W., de Jeu, R., van der Schalie, R., Scanlon, T., Teubner, I., and Forkel, M.: The global long-term microwave
451   Vegetation Optical Depth Climate Archive (VODCA), Earth System Science Data, 12, 177–177, 2020.

452 Naeimi, V., Scipal, K., Bartalis, Z., Hasenauer, S., and Wagner, W.: An Improved Soil Moisture Retrieval Algorithm for
453   ERS and METOP Scatterometer Observations, IEEE Transactions on Geoscience and Remote Sensing, 47, 1999–2013,
454   https://doi.org/10.1109/TGRS.2008.2011617, 2009.

455 Nemani, R. R., Keeling, C. D., Hashimoto, H., Jolly, W. M., Piper, S. C., Tucker, C. J., Myneni, R. B., and Running, S. W.: Climate-driven
456   increases in global terrestrial net primary production from 1982 to 1999, Science, 300, 1560–1563, 2003.

457 Oliveira, R., Bezerra, L., Davidson, E., Pinto, F., Klink, C., Nepstad, D., and Moreira, A.: Deep root function in soil water dynamics in
458   cerrado savannas of central Brazil, Functional Ecology, 19, 574–581, 2005.

459 Olson, D. M., Dinerstein, E., Wikramanayake, E. D., Burgess, N. D., Powell, G. V., Underwood, E. C., D'amico, J. A., Itoua, I., Strand,
460   H. E., Morrison, J. C., et al.: Terrestrial Ecoregions of the World: A New Map of Life on EarthA new global map of terrestrial ecoregions
461   provides an innovative tool for conserving biodiversity, BioScience, 51, 933–938, 2001.

462 Owe, M., de Jeu, R., and Walker, J.: A methodology for surface soil moisture and vegetation optical depth retrieval using the microwave
463   polarization difference index, IEEE Transactions on Geoscience and Remote Sensing, 39, 1643–1654, http://ieeexplore.ieee.org/xpls/abs_
464   all.jsp?arnumber=942542, 2001.

465 Panisset, J. S., Libonati, R., Gouveia, C. M. P., Machado-Silva, F., França, D. A., França, J. R. A., and Peres, L. F.: Contrasting patterns of
466   the extreme drought episodes of 2005, 2010 and 2015 in the Amazon Basin, International Journal of Climatology, 38, 1096–1104, 2018.

467 Peel, M. C., Finlayson, B. L., and McMahon, T. A.: Updated world map of the Köppen-Geiger climate classification, Hydrology and Earth
468   System Sciences Discussions, 4, 439–473, 2007.

469 Pfeil, I., Wagner, W., Forkel, M., Dorigo, W., and Vreugdenhil, M.: Does ASCAT observe the spring reactivation in temperate deciduous
470   broadleaf forests?, Remote Sensing of Environment, 250, 112 042, 2020.

471 Rao, K., Anderegg, W. R. L., Sala, A., Martínez-Vilalta, J., and Konings, A. G.: Satellite-based vegetation optical depth as an indicator of
472   drought-driven tree mortality, Remote Sensing of Environment, 227, 125–136, https://doi.org/10.1016/j.rse.2019.03.026, 2019.

473 Romatschke, U. and Houze Jr, R. A.: Characteristics of precipitating convective systems accounting for the summer rainfall of tropical and
474   subtropical South America, Journal of Hydrometeorology, 14, 25–46, 2013.

475 Saatchi, S., Asefi-Najafabady, S., Malhi, Y., Aragão, L. E., Anderson, L. O., Myneni, R. B., and Nemani, R.: Persistent effects of a severe
476   drought on Amazonian forest canopy, Proceedings of the National Academy of Sciences, 110, 565–570, 2013.

477 Schroeder, R., McDonald, K. C., Azarderakhsh, M., and Zimmermann, R.: ASCAT MetOp-A diurnal backscatter observations of recent
478   vegetation drought patterns over the contiguous US: An assessment of spatial extent and relationship with precipitation and crop yield,
479   Remote sensing of environment, 177, 153–159, publisher: Elsevier, 2016.

480 Sheffield, J., Goteti, G., and Wood, E. F.: Development of a 50-year high-resolution global dataset of meteorological forcings for land surface
481   modeling, Journal of climate, 19, 3088–3111, 2006.

482 Soares, B. S., Nepstad, D. C., Curran, L. M., Cerqueira, G. C., Garcia, R. A., Ramos, C. A., Voll, E., McDonald, A., Lefebvre, P., and
483   Schlesinger, P.: Modelling conservation in the Amazon basin, Nature, 440, 520–523, 2006.

484 Steele-Dunne, S. C., Friesen, J., and van de Giesen, N.: Using diurnal variation in backscatter to detect vegetation water stress, IEEE
485   Transactions on Geoscience and Remote Sensing, 50, 2618–2629, 2012.

486 Steele-Dunne, S. C., McNairn, H., Monsivais-Huertero, A., Judge, J., Liu, P.-W., and Papathanassiou, K.: Radar remote sensing of agricultural
487   canopies: A review, IEEE Journal of Selected Topics in Applied Earth Observations and Remote Sensing, 10, 2249–2273, 2017.

488 Steele-Dunne, S. C., Hahn, S., Wagner, W., and Vreugdenhil, M.: Investigating vegetation water dynamics and drought using Metop ASCAT
489   over the North American Grasslands, Remote Sensing of Environment, 224, 219–235, 2019.

490 Stoffelen, A., Aaboe, S., Calvet, J.-C., Cotton, J., De Chiara, G., Saldana, J. F., Mouche, A. A., Portabella, M., Scipal, K., and Wagner,
491   W.: Scientific developments and the EPS-SG scatterometer, IEEE Journal of Selected Topics in Applied Earth Observations and Remote
492   Sensing, 10, 2086–2097, 2017.

493 Swenson, S. and Wahr, J.: Post-processing removal of correlated errors in GRACE data, Geophysical Research Letters, 33, 2006.

494 Templ, B., Koch, E., Bolmgren, K., Ungersböck, M., Paul, A., Scheifinger, H., Busto, M., Chmielewski, F.-M., Hájková, L., Hodzić, S., et al.:
495   Pan European Phenological database (PEP725): a single point of access for European data, International journal of biometeorology, 62,
496   1109–1113, 2018.

497 Teubner, I., Forkel, M., Jung, M., Liu, Y., Miralles, D., Parinussa, R., van der Schalie, R., Vreugdenhil, M., Schwalm, C., Tramontana, G.,
498   Camps-Valls, G., and Dorigo, W.: Assessing the relationship between microwave vegetation optical depth and gross primary production,
499   International Journal of Applied Earth Observation and Geoinformation, 65, 79–91, https://doi.org/10.1016/j.jag.2017.10.006, 2018.

500 Teubner, I., Forkel, M., Camps-Valls, G., Jung, M., Miralles, D., Tramontana, G., van der Schalie, R., Vreugdenhil, M., Mösinger, L., and
501   Dorigo, W.: A carbon sink-driven approach to estimate gross primary production from microwave satellite observations, Remote Sensing
502   of Environment, 229, 100–113, https://doi.org/10.1016/j.rse.2019.04.022, 2019.

503 Vreugdenhil, M., Dorigo, W. A., Wagner, W., De Jeu, R. A., Hahn, S., and Van Marle, M. J.: Analyzing the vegetation parameterization in
504   the TU-Wien ASCAT soil moisture retrieval, IEEE Transactions on Geoscience and Remote Sensing, 54, 3513–3531, 2016.

505 Wagner, F. H., Hérault, B., Bonal, D., Stahl, C., Anderson, L. O., Baker, T. R., Sebastian Becker, G., Beeckman, H., D Souza, B., Cesar Boto-
506   sso, P., et al.: Climate seasonality limits leaf carbon assimilation and wood productivity in tropical forests, Biogeosciences, 13, 2537–2562,
507   2016.

508 Wagner, W., Lemoine, G., Borgeaud, M., and Rott, H.: A study of vegetation cover effects on ERS scatterometer data, IEEE Transactions on
509   Geoscience and Remote Sensing, 37, 938–948, 1999.

510 Wagner, W., Hahn, S., Kidd, R., Melzer, T., Bartalis, Z., Hasenauer, S., Figa-Saldaña, J., de Rosnay, P., Jann, A., Schneider, S., Komma,
511   J., Kubu, G., Brugger, K., Aubrecht, C., Züger, J., Gangkofner, U., Kienberger, S., Brocca, L., Wang, Y., Blöschl, G., Eitzinger, J.,
512   Steinnocher, K., Zeil, P., and Rubel, F.: The ASCAT Soil Moisture Product: A Review of Its Specifications, Validation Results, and
513   Emerging Applications, Meteorologische Zeitschrift, 22, 5–33, https://doi.org/10.1127/0941-2948/2013/0399, 2013.

514 Wahr, J., Molenaar, M., and Bryan, F.: Time variability of the Earth's gravity field: Hydrological and oceanic effects and their possible
515   detection using GRACE, Journal of Geophysical Research: Solid Earth, 103, 30 205–30 229, 1998.

516 Wismann, V. R., Boehnke, K., and Schmullius, C.: Monitoring ecological dynamics in Africa with the ERS-1 scatterometer, in: 1995 Inter-
517   national Geoscience and Remote Sensing Symposium, IGARSS'95. Quantitative Remote Sensing for Science and Applications, vol. 2,
518   pp. 1523–1525, IEEE, 1995.

519 Woodhouse, I. H., van der Sanden, J. J., and Hoekman, D. H.: Scatterometer observations of seasonal backscatter variation over tropical rain
520   forest, IEEE transactions on geoscience and remote sensing, 37, 859–861, publisher: IEEE, 1999.

521 Wright, S. J. and Van Schaik, C. P.: Light and the phenology of tropical trees, The American Naturalist, 143, 192–199, 1994.

522 WWF: Terrestrial Ecoregions | Biome Categories | WWF, https://www.worldwildlife.org/biome-categories/terrestrial-ecoregions, 2019.